Hyperfine Interact
DOI 10.1007/s10751-012-0654-z

Defect-fluorite oxides: Ln (Eu and Gd) Mössbauer study coupled with new defect-crystal-chemistry model

A. Nakamura · N. Igawa · Y. Okamoto · J. Wang · Y. Hinatsu · M. Takahashi · M. Takeda

Received: 13 September 2012 / Accepted: 18 September 2012

Abstract A recently proposed lattice-parameter (a_0(ss)) model for parent fluorite-type MO_2-$LnO_{1.5}$ solid solutions (M^{4+}=Ce and Th; Ln^{3+}=lanthanide) has been extended to more complex $LnO_{1.5}$-stabilized zirconia (hafnia) (M^{4+}=Zr(Hf)) with pyrochlore-type ordering and its-associated broad a_0(ss) hump, using key Ln (Eu and Gd)-Mössbauer and related local-structure data.

Keywords Stabilized zirconia (hafnia) · Pyrochlore · Lattice-parameter model · Non-random local structure · Metal-oxygen bond length · Ln-Mössbauer · NMR and EXAFS spectroscopy · Extended bond valence sum rule

Submitted to Hyperfine Interactions as ISIAME2012 (Dalian) Proceedings paper (invited lecture).

A. Nakamura (✉)
Advanced Science Research Center, Japan Atomic Energy Agency,
Tokai, Naka, Ibaraki 319-1195, Japan
e-mail: nakamura.akio@jaea.go.jp

N. Igawa · Y. Okamoto
Quantum Beam Science Directorate, Japan Atomic Energy Agency,
Tokai, Naka, Ibaraki 319-1195, Japan

J. Wang
Dalian Institute of Chemical Physics,
Chinese Academy of Science, Dalian 116023, China

Y. Hinatsu
Department of Chemistry, Hokkaido University,
Sapporo 160-0810 Hokkaido, Japan

M. Takahashi · M. Takeda
Department of Chemistry, Toho University,
Funabashi, Chiba 274-8510, Japan

Published online: 01 November 2012

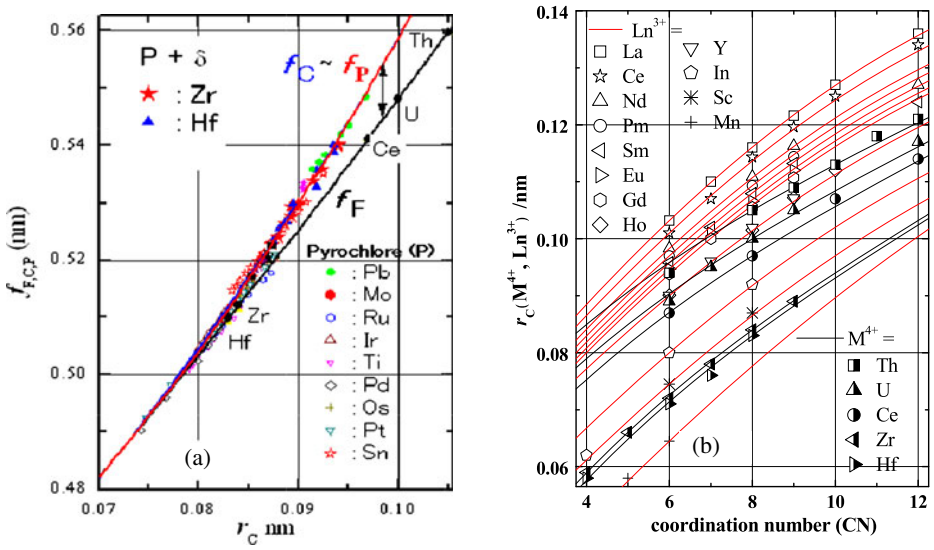

Fig. 1 **a** $f_F = a_0(F)$, $f_C = a_0(C)/2$ and $f_{P(\delta)} = a_0(P)/2$ vs. $r_C(ss)$ plot for F MO_2, C $LnO_{1.5}$ and P(δ) $Zr(Hf)_2Ln_2O_7$ and **b** Shannon's $r_C(M^{4+}, Ln^{3+})$ vs. CN plot and their systematized curves

1 Introduction

As a new approach to the controversial defect structure of defect-fluorite (DF) oxides, i.e., oxygen-vacancy (V_O) type $M_{1-y}Ln_yO_{2-y/2}$ solid solutions (ss) (often shortened as M-Ln below) between fluorite (F)-type MO_2 (M^{4+}=Zr, Hf, Ce, Th, U etc) and its V_O-ordered C-type $LnO_{1.5}$ (Ln^{3+}=La-Lu, Sc, Y etc) with doubled lattice parameter of $a_0(C) = 2a_0(F)$, one of the authors (AN) has lately proposed a defect-crystal-chemistry lattice-parameter (a_0(ss)) model for parent F-type M-Lns (M^{4+}=Ce and Th; Ln^{3+}=La-Y) that can provide a unified picture of non-Vegardianity and non-random defect structure as two sides of distortion-dilation phenomenon of C $LnO_{1.5}$ relative to F MO_2; $f_F\,(=a_0(F)) < f_C\,(=a_0(C)/2)$ in Fig. 1a [1, 2]. (Figure 1a also includes $f_P = a_0(P)/2$ data for various pyrochlores). It has a generalized Vegard-law (VL) a_0(ss) formula of:

$$a_0\,(\mathrm{ss}) = (1-y)\cdot f_F\,(r_C\,(\mathrm{ss})) + y\cdot f_C\,(r_C\,(\mathrm{ss})) \quad \text{at} \tag{1}$$

$$r_C\,(\mathrm{ss}) = (1-y)\cdot r_C\left(M^{4+}\right) + y\cdot r_C\left(Ln^{3+}\right). \tag{2}$$

Namely, the intercept of a vertical straight line at the average cation radius r_C(ss) with the f_F or f_C gives the system's a_0, if this were at CN = 8 or 6 of the hypothetic F M'O_2 or C Ln'$O_{1.5}$ at its r_C(ss), respectively. As the actual system is at CN = 8–2y as a $(1-y)\cdot$M'$O_2 + y\cdot$Ln'$O_{1.5}$ mixture, its a_0(ss) is given by their arithmetic y average (1) rather than the actual end members (MO_2 and $LnO_{1.5}$) as with the conventional Vegard law (VL):

$$a_0\,(\mathrm{VL}) = (1-y)\cdot f_F\left(r_C\left(M^{4+}\right)(\mathrm{VIII})\right) + y\cdot f_C\left(\left(r_C\left(Ln^{3+}\right)(\mathrm{VI})\right)\right) \quad (\text{linear in } y). \tag{3}$$

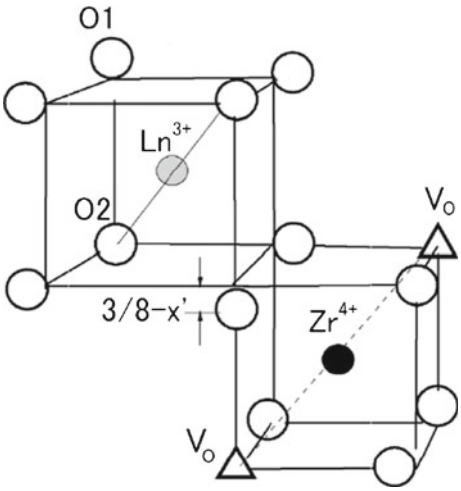

Fig. 2 Ideal pyrochlore (P) structure of $Ln_2Zr_2O_7$ with two short apical (Ln-O2) bonds and six longer (Ln-O1) bonds caused by the shift of O1 positional parameter x' from 0.375 for the fluorite (F) structure

f_F and f_C in (1) and $r_C(M^{4+}, Ln^{3+})$ in (2) are the two sets of pair equations necessary for their a_0(ss) analysis, all of which are drawn in Fig. 1a–b and are already given in [1].

The proposed 'systematized' Shannon's $r_C(M^{4+}, Ln^{3+})$ curves as a function of oxygen coordination number (CN) in Fig. 1b enable not only r_C(ss) (2) to be calculated for the whole $0 \leq y \leq 1.0$ ($8 \geq CN \geq 6$) range but also their non-random $CN(Ln^{3+}, M^{4+})$ to be extracted from the a_0(ss)-data analysis. As detailed in [1], their non-random $CN(Ln^{3+}, M^{4+})$ data clarified the contrastive coupled non-Vegardianity ($\Delta a_0(ss)=a_0(ss)$-$a_0(VL)$)—non-random defect structure of the M^{4+}=Th and Ce: the strongly Ln^{3+}-Vo associative ($CN(Ln^{3+})<<(8–2y)<<CN(Th^{4+})$) largely non-Vegardian former ($\Delta a_0(ss)>>0$) with the largest host Th^{4+} ($r_C(VIII) = 0.105$ nm) vs. the only weakly Ln^{3+}-Vo associative to near-random less non-Vegardian latter with the smaller host Ce^{4+} ($r_C(VIII) = 0.097$ nm), consistently with their reported local-structure and oxygen conductivity (σ(ion)) etc data. Further in [2], full use of these $CN(Ln^{3+}, M^{4+})$ data has enabled not only to derive all the mutually non-randomly coordinated cation ↔ anion concentrations but also to give a new σ(ion)(maximum) description in their low y range.

This success of the F-C binary model means that parent F-type M^{4+}=Th and Ce are indeed the F MO_2–C $LnO_{1.5}$ binary systems, and by this very nature it would not be applicable to much smaller-M^{4+}-based stabilized zirconia (hafnia) (SZ(SH); $r_C(Zr(Hf)^{4+}(VIII)) = 0.084$ (0.083) nm) with pyrochlore (P) (or δ)-type intermediate ordering and its associated broad a_0(ss) hump [1, 2]. The ideal P $M_2Ln_2O_7$ at $y = 0.50$ (Fig. 2) has an uniquely long-range ordered structure in which smaller M^{4+} and larger Ln^{3+} are CN=VI and VIII, respectively, totally switched from F MO_2 (CN=VIII) and C $LnO_{1.5}$ (CN=VI). a_0(P) data in Fig. 1a indicate that Ps at $y = 0.50$ are already near equally largely distortion-dilated to C $LnO_{1.5}$ at $y = 1.0$. The $f_P = a_0(P)/2$, thus set equal to f_C, is written below for its different r_C definition;

$$f_P(r_C)\,(=f_C(r_C)) = a_0(P)/2 \quad \left(\text{for } r_C = \left\{r_C\left(Ln^{3+}\right)(VIII) + r_C\left(M^{4+}\right)(VI)\right\}/2\right). \quad (4)$$

For SZ(SH)s such P(δ)-type extra distortional dilation is to be incorporated into the model. To propose such extended a_0(ss) model is the aim of this paper.

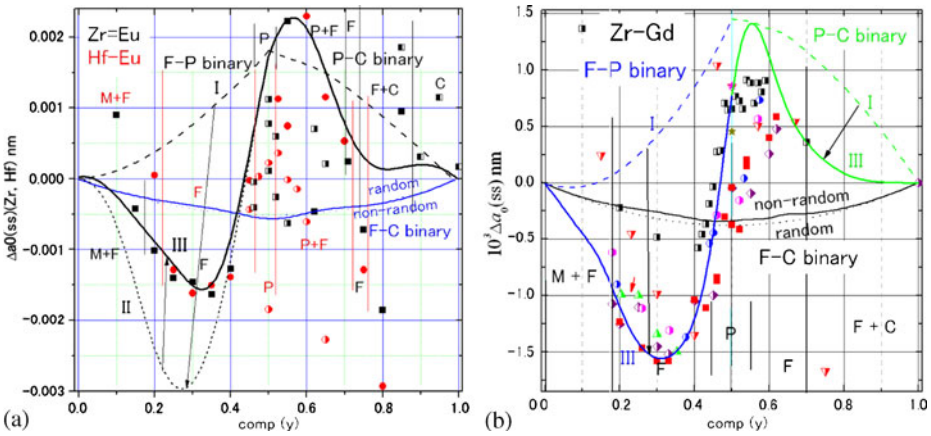

Fig. 3 Δa_0(ss) data and their model curves in Zr-Eu and Hf-Eu (**a**) and in Zr-Gd (**b**)

2 Lattice-parameter and local-structure data

Figure 3 summarizes the results of our stepwise a_0(ss)-model extension for Zr-Eu and Hf-Eu (**a**) and Zr-Gd (**b**) as Δa_0(ss)-y plot. These three are chosen here, for they have key Ln (Eu, Gd) Mössbauer-structure and detailed a_0(ss) data. How to reach their most reasonable F-P-C ternary a_0(ss) model-**III** whose Δa_0(ss) curves are drawn in thickest solid line is the main theme here. In sharp contrast to a simply positively Δa_0(ss)(>0) M^{4+} = Th and Ce, these SZ(SH)s exhibit strongly-sigmoid both negative(<0) to positive(>0) Δa_0(ss), initially decreasing to a deep dip at $y \sim 0.33$, then turning to increase sharply to a peak at $y \sim 0.50$–0.55, and lastly decreasing slowly in the $y > \sim 0.55$ till the DF/C phase boundary. The total dip-peak Δa_0(ss) change ($\sim$2–3·10^{-3} nm) here is almost comparable to Δa_0(ss)(max)s of many Ce-Lns.

As clarified in [3, 4], the major $\sim 0.33 \leq y \leq \sim 0.60$–$70$ region over which a broad Δa_0(ss) hump extends is either the long- or short-range ordered pyrochlore (P) phase, the former macroscopic P forming only in the narrow middle $0.45 \leq y \leq 0.55$ range. The outer 'XRD apparently-disordered' DF phase in the $\sim 0.33 \leq y < \sim 0.45$ range over which a steep Δa_0(ss) increase occurs is thus the growing short-range-ordered P-type phase, as the ^{155}Gd-Mössbauer quadrupole-splitting (QS) and Debye-temperature (Θ_D) data of Zr-Gd indicate (Fig. 4a–b) [4–8]. Although the QS data show a near continuous growth of P-type distorted Gd(VIII)-8O bond anisotropy (Fig. 2), the Θ_D data clearly reveal an abrupt increase of the structural integrity first at $y \sim 0.33$ (where P-type short-range ordering starts) and then at $y \sim 0.45$ (where the macroscopic P forms). The $y \sim 0.33$ just coincides with the σ(ion) turning point from down (↓) to up (↑) trend to the 2nd σ(ion)(max) at the ideal P at $y = 0.50$ [4].

^{151}Eu-Mössbauer isomer-shift (IS(Eu^{3+})) data on M-Eus (M^{4+} = Hf, Zr, Ce, Th and U) (Fig. 5) [4, 9, 10] give a decisive evidence that such macroscopic distortional dilation of a_0(ss) for $y = 0.33 \rightarrow 0.50$ in Fig. 3 is intimately coupled with that of the microscopic cation-O^{2-} bond-length (BL). In light of the well-known correlation in oxides that higher the IS(Eu^{3+}) shorter the BL(Eu^{3+}-O), these data indicate that

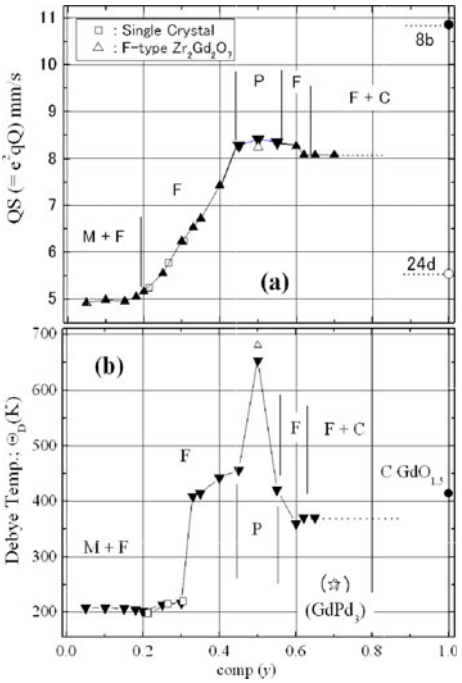

Fig. 4 QS (**a**) and Θ_D (**b**) data in $Zr_{1-y}Gd_yO_{2-y/2}$ system

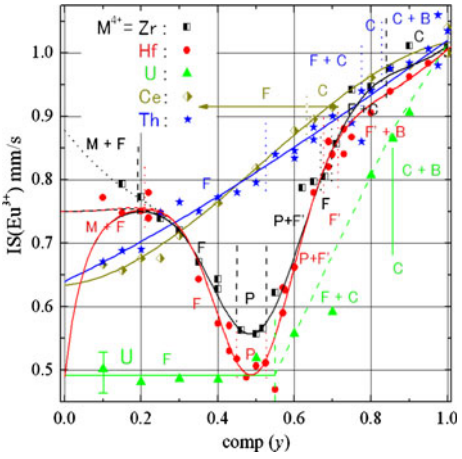

Fig. 5 IS(Eu^{3+}) vs. *y* plot for M-Eu (M^{4+}=Hf, Zr, Ce, Th and U) (EuF_3 reference)

again in sharp contrast to Th-Eu and Ce-Eu (see also [11], Nakamura et al., to be published in 2013) both Zr-Eu and Hf-Eu exhibit a similar rapid average BL(Eu(VIII)-O) dilation of its P-type distorted oxygen cube (BL(Eu(VIII)-2O2)<BL(Eu(VIII)-6O1) in Fig. 2), taking the longest average BL(Eu(VIII)-O)s at the most-ordered and anisotropic ideal-P $Zr_2(Hf)_2Eu_2O_7$ at $y = 0.50$. It is also apparent that more ordered and more distorted P $Eu_2Hf_2O_7$ with the smaller a_0(ss) $\sim$ 0.523 nm has the longer (i.e., locally more distortion-dilated) average BL(Eu(VIII)-O) than P $Eu_2Zr_2O_7$ with the larger a_0(ss) $\sim$ 0.524 nm.

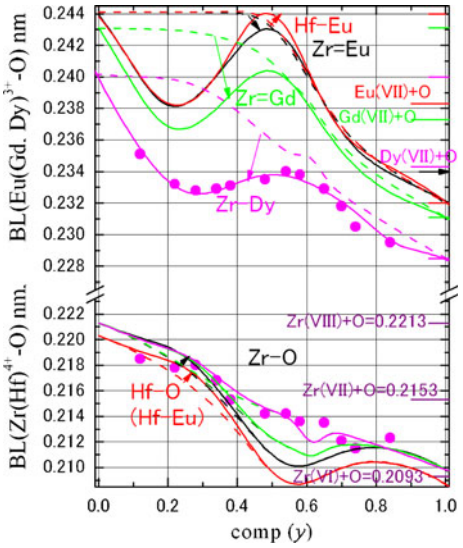

Fig. 6 BL(Ln-O, Zr(Hf)-O) vs. y plot in several SZ(SH)s. Shannon's r_C(Ln,Zr(Hf))+r_a(O); *dashed line*, Eu-Mössbauer and EXAFS based BL(Ln-O, Zr(Hf)-O); *solid line*

The near constant BL((Eu(VIII)-O) ~ 0.49 mm/s up to the fully oxidized $U^{5+}_{0.5}Eu^{3+}_{0.5}O_2$ in the $y \leq 0.50$ and the BL((Eu(VI)-O) in C $EuO_{1.5}$ give two reference points in Fig. 5;

$$\text{(i)} \quad \mathrm{BL}\left(\mathrm{Eu}^{3+}(\mathrm{VIII}) - \mathrm{O}\right) = 0.2439\,(\sim 0.2446)\ \text{nm at IS}\left(\mathrm{Eu}^{3+}(\mathrm{VIII})\right) = 0.49\ \text{mm/s} \tag{5a}$$

$$\text{(ii)} \quad \mathrm{BL}\left(\mathrm{Eu}^{3+}(\mathrm{VI}) - \mathrm{O}\right) = 0.232\,(\sim 0.234)\ \text{nm at IS}\left(\mathrm{Eu}^{3+}(\mathrm{VI})\right) = 1.025\ \text{mm/s}. \tag{5b}$$

From these one can derive the most reasonable BL-IS correlation in these DF oxides;

$$\mathrm{BL}\left(\mathrm{Eu}^{3+} - \mathrm{O}\right) = \left\{11.18 - \mathrm{IS}\left(\mathrm{Eu}^{3+}\right)\right\}/43.75, \tag{6}$$

(See Nakamura et al., to be published in 2013 for details of (6) derivation and BL((Eu^{3+}(VIII, VI)-O) data problem in each parenthesis in (5a–b)).

Inserting both IS(Eu^{3+})-y curves in Fig. 5 in solid red and black line into (6), we can derive both BL(Eu^{3+}-O)-y curves as drawn in Fig. 6. This shows that both BL(Eu^{3+}-O)s indeed increase (distortion dilated) sharply with y from a common BL(Eu^{3+}-O)(min) ~ 0.2382 nm at $y \sim 0.20$–0.23 to the respective BL(Eu^{3+}-O)(max) at $y \sim 0.50$, despite the obvious fact that both CN(Eu^{3+}) remain at the highest CN ~ 8 level over the entire $\sim 0.20 \leq y \leq \sim 0.50$ range, as confirmed in Fig. 7, summarizing their CN(Ln^{3+}, Zr(Hf)$^{4+}$) behavior in reference to reported ^{89}Y MAS-NMR CN(Y^{3+}, Zr^{4+}) data in YSZ [12–14]. Other data used in Fig. 7 are: CN(Gd^{3+}) = 7.6 and CN(Zr^{4+}) = 6.4 in P $Zr_2Gd_2O_7$ at $y = 0.50$ in the single-crystal XRD study [15], which clarified that even at $y = 0.50$ decreasing the ionic-radii mismatch, r_C(Ln^{3+})(VI)/r_C(M^{4+})(VIII) = 1.141(Hf-Eu) → 1.127(Zr-Eu) → 1.1167(Zr-Gd) → 1.071(Zr-Y), promotes the oxygen-sublattice

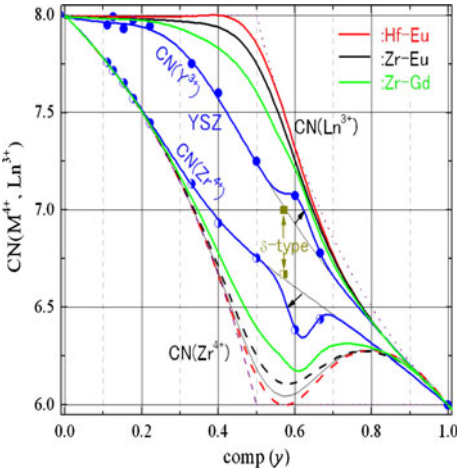

Fig. 7 ^{89}Y-MAS-NMR $CN(Y^{3+}, Zr^{4+})$ data of YSZ and simulated $CN(Ln^{3+}, Zr(Hf)^{4+})$ curves of Hf-Eu, Zr-Eu and Zr-Gd

disorder in P in Fig. 2; $O1(48f) + V_O(8a) \leftrightarrow V_O(48f) + Oi(8a)$. In fact, both SZ and SH with the smaller Ln^{3+}s than Gd^{3+} form not P- but δ-type ordered phase, the ideal δ $Zr(Hf)_3Ln_4O_{12}$ $(=[Zr(Hf)^{4+}]_{VI}[Zr(Hf)_2^{4+}Ln_4^{3+}]_{VII}O_{12})$ at $y = 0.5741$ being much less $Zr(Hf)^{4+}$-V_O associative; $CN(Zr(Hf)^{4+}) = 6.67 < CN(Ln^{3+}) = 7$, as depicted there.

Although the actual $BL(Eu^{3+}$-O) behavior in the M/DF di-phasic $y <\sim 0.20$ range is not clear in Fig. 5, the onset of both $BL(Eu^{3+}$-O) minima at $y \sim 0.20$–0.23 is reinforced by our latest detailed EXAFS $BL(Dy^{3+}$-O) (and $BL(Zr^{4+}$-O)) data in Zr-Dy also plotted in Fig. 6: The $BL(Dy^{3+}$-O) data show an initial sharp decrease from the Shannon's $BL(Dy^{3+}(VIII)$-O) ~ 0.240 nm at $y = 0$ to a minimum ~ 0.2328 nm at $y \sim 0.30$ that is even shorter than Shannon's $BL(Dy^{3+}(VII)$-O) ~ 0.2342 nm, and then increase gradually to a shallow maximum at $y \sim 0.50$–0.55. The global $BL(Dy^{3+}$-O) shape in Zr-Dy is a kind of milder-max version at $y \sim 0.50$ of those of Zr-Eu and Hf-Eu. For comparison, corresponding Shannon's $BL(Ln^{3+}$-O, $Zr(Hf)^{4+}$-O) curves are drawn there in dashed line by inserting each $CN(Ln^{3+}, Zr(Hf)^{4+})$ data (Fig. 7) into systematized Shannon's $r_C(Ln^{3+}, Zr(Hf)^{4+})$ curves (Fig. 1b) and adding them $r_a(O) = 0.1373$ nm [1]; $BL(Ln^{3+}$-O, $Zr(Hf)^{4+}$-O) = $r_C(Ln^{3+}, Zr(Hf)^{4+}) + 0.1373$ nm. For Zr-Dy, since $r_C(Dy^{3+})(VI) \sim 0.0912$ nm is much closer to $r_C(Y^{3+})(VI) \sim 0.090$ nm than $r_C(Gd^{3+})(VI) \sim 0.0938$ nm, the $CN(Y^{3+}, Zr^{4+})$ curves of Zr-Y (YSZ) in Fig. 7 were used for this purpose. Whereas, the calculated Shannon's $BL(Zr^{4+}$-O) curve of Zr-Dy (in pink) shows relatively good agreement with the EXAFS $BL(Zr^{4+}$-O) data. Finally, the sigmoid $BL(Gd^{3+}$-O) curve of Zr-Gd was drawn there (in green) so as to have a mixed character of those of the both-side neighbors (Zr-Eu and Zr-Dy) and extrapolate to the Shannon's $BL(Gd^{3+}(VIII)$-O) = 0.2431 nm at $y \rightarrow 0$.

Summarizing the above results, it is reasonably concluded that in the firstly cubic-F stabilized $\sim 0.20 \leq y \leq\sim 0.33$ range these SZ(SH)s take a peculiar $BL(Ln^{3+}$-O) minimum that is almost equal to or even smaller than each Shannon's $BL(Ln^{3+}(VII)$-O), being far reduced from each Shannon's $BL(Ln^{3+}(VIII)$-O) for $CN(Ln^{3+}) \sim 8$ (Fig. 7). It is as if too large Ln^{3+} and too small $Zr(Hf)^{4+}$ are striving together to

form their common stabilized cubic-F solid solution by making themselves as small and large as possible, respectively.

3 Extended defect-crystal-chemistry lattice-parameter model

As Zr-Eu and Hf-Eu have similarly 'scattered' Δa_0(ss) data in Fig. 3a, the model extension is made only for the former and Zr-Gd in Fig. 3b. Firstly, the F-C binary model in (1–2) is applied with above-introduced $r_C(Ln^{3+}, Zr(Hf)^{4+})$(Shannon) in Fig. 1b. The results drawn in Fig. 3a–b indicate that this, either random ($CN(Ln^{3+}) = CN(Zr^{4+}) = 8–2y$) or non-random, cannot at all reproduce their such strongly sigmoid Δa_0(ss), giving only weakly negative Δa_0(ss) (<0) curves.

This is quite natural from the above-clarified fact that SZ(SH)s have P-based another unique distortional dilation—non-randomness coupling mechanism. So, the a_0(ss) formula is modified to the following F-P-C ternary type;

$$a_0\,(\text{ss})\,(\text{F}-\text{P}) = (1-2y)\cdot f_\text{F} + 2y\cdot f_\text{P} \quad (\text{for } 0 \le y \le 0.50)\,. \tag{7a}$$

$$a_0\,(\text{ss})\,(\text{P}-\text{C}) = 2\,(1-y)\cdot f_\text{P} + (2\,y-1)\cdot f_\text{C} = f_\text{C} \quad (\text{for } 0.50 \le y \le 1.0)\,, \tag{7b}$$

The composition ratio of $(1–2y)/2y$ for the F/P hybrid phase in (7a) results from the fact that the system completely switches from F MO_2 at $y = 0$ to P $M_{0.5}Ln_{0.5}O_{1.75}$ at $y = 0.50$. The same also applies to the P/C hybrid phase for the $y \ge 0.50$ range in (7b), where $f_P = f_C$ in (4) (Fig. 1a) makes its a_0(ss) after all equal to f_C itself. The derived model-**I** Δa_0(ss) curves with non-random $r_C(Ln^{3+}, Zr(Hf)^{4+})$(Shannon) curves are simply positively Δa_0(ss) (>0) over the entire range, because $r_C(Ln^{3+}, Zr(Hf)^{4+})$(Shannon) curves do not incorporate the marked $r_C(Ln^{3+})$ reduction over the $y = 0.20$–30 range in Fig. 6.

So, the model-**II** attempt taking this $r_C(Ln^{3+})$ reduction into account was made for Zr-Eu in Fig. 3a, resulting in the excessive lowering of the Δa_0(ss) curve to too deep a dip at $y \sim 0.027$. This implies that in response to such $r_C(Ln^{3+})$ reduction the counteracting $r_C(Zr^{4+})$ expansion should be occurring here too. The latter was incorporated in the Model-**III** by giving a smaller but relatively wide $r_C(Zr^{4+})$ hump over the initial $\sim 0.10 \le y \le 0.40$ range (as indicated by arrow) in Fig. 6. As seen in Fig. 3a–b one can then obtain both model-**III** Δa_0(ss) curves reproducing well the respective data.

These results indicate that a largely-distorted monoclinic Zr(Hf)O_2 with CN ~ 7 at $y = 0$ and C-type $LnO_{1.5}$ (CN=VI) at $y = 1.0$, being mutually too small and too large a partner, respectively, collaborate to form their common-platform 'stabilized solid solution', even taking off their casual individual clothes of Shannon's $r_C(Zr^{4+}, Ln^{3+})$ (Fig. 1b). This would be because it is a more comfortable place for the host ZrO_2 (but appears not necessarily so for the dopant $LnO_{1.5}$ from the low Θ_D(Gd) ~ 200 °C there (Fig. 4b)). First after the $CN(Zr^{4+})$ has decreased to ~7 at $y \sim 0.33$ (Fig. 7), the system starts moving to the next-step collective P-type short ordering (toward the $CN(Zr^{4+}) \sim 6$ at the ideal P at $y = 0.50$), exerting coupled macroscopic-a_0(ss) and microscopic-r_C distortion dilation to realize most comfortable individual rooms for both cations (16d and 16c sites in P (Fig. 2)).

These SZ(SH)s seem to be rare solid solutions that have so largely and systematically mutually expanded and shrunken host and dopant cations, respectively,

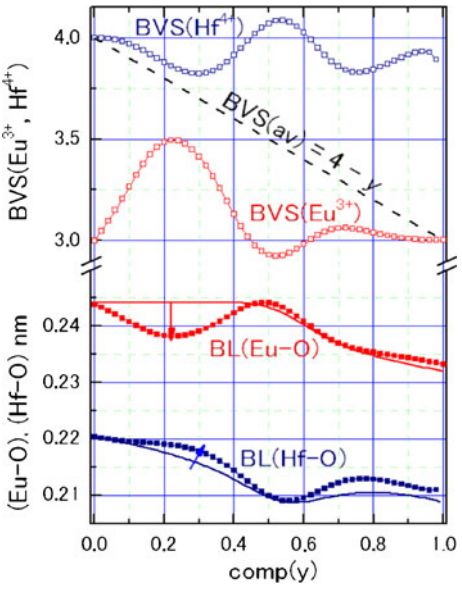

Fig. 8 Extended BVS-rule calculations in Hf-Eu. The arrow indicates each Shannonian → Non-Shannonian BL change

so obviously taking off each usual Shannon's ionic radius. Then, the more global concept working here seems to be the 'extended bond-valence sum (BVS) rule', as an generalization of the original one for each cation by Brown [16] to the two kinds of cations coexisting in the same crystalline lattice. Where, each bond's unit s(i) is defined by the parameter R_0 in, e.g., $\mathrm{s}\left(\mathrm{Ln}^{3+}\right) = \exp\left\{\left(R_0 - \mathrm{BL}\left(\mathrm{Ln}^{3+} - \mathrm{O}\right)\right)/0.037\right\}$, and its summation over all the coordinating O^{2-}s (bond valence sum (BVS)) is assumed to give the valence of the central cation, BVS $=\sum$s(i). In the present $\mathrm{M}_{1-y}\mathrm{Ln}_y\mathrm{O}_{2-y/2}$ the extended BVS rule says that;

$$\mathrm{BVS\,(av)} = (1-y)\cdot \mathrm{BVS}\left(\mathrm{M}^{4+}\right) + y\cdot \mathrm{BVS}\left(\mathrm{Ln}^{3+}\right) = 2\cdot\left(2-y/2\right) = 4-y, \qquad (8)$$

where, assuming the presence of only a single kind of either BL(M^{4+}-O) or BL(Ln^{3+}-O) bond around each cation as a first approximation, it is set;

$$\mathrm{BVS}\left(\mathrm{M}^{4+}\right) = \sum \mathrm{s}\left(\mathrm{M}^{4+}\right) = \mathrm{CN}\left(\mathrm{M}^{4+}\right)\cdot \exp\left\{\left(R_0\left(\mathrm{M}^{4+}\right) - \mathrm{BL}\left(\mathrm{M}^{4+} - \mathrm{O}\right)\right)/0.037\right\} \qquad (9a)$$

$$\mathrm{BVS}\left(\mathrm{Ln}^{3+}\right) = \sum \mathrm{s}\left(\mathrm{Ln}^{3+}\right) = \mathrm{CN}\left(\mathrm{Ln}^{3+}\right)\cdot \exp\left\{\left(R_0\left(\mathrm{Ln}^{3+}\right) - \mathrm{BL}\left(\mathrm{Ln}^{3+} - \mathrm{O}\right)\right)/0.037\right\}. \qquad (9b)$$

Equation (8) is the electrical neutrality condition of the system expressed in terms of the BVS model. Applying (8) and (9a–b) to the M^{4+}=Hf and Ln^{3+}=Eu by using $R_0(\mathrm{Hf}^{4+}) = 0.19466$ and $R_0(\mathrm{Eu}^{3+}) = 0.2076$ [16], BVS(Hf^{4+}, Eu^{3+}) and BL(Hf^{4+}-O) curves in Hf-Eu are calculated for its known CN(Eu^{3+}, Hf^{4+}) (Fig. 7) and BL(Eu^{3+}-O) (Fig. 6), and are drawn in Fig. 8. The results demonstrate that, when the dopant Ln^{3+} exhibits a strongly non-Shannonian BL(Eu^{3+}-O) dip, the host Hf^{4+} too exhibits a converse non-Shannonian BL(Hf^{4+}-O) hump, as the above a_0(ss)-model analysis requires. Namely, these M^{4+}-Ln^{3+} solid solutions are performing coupled

non-random local-r_C and macroscopic-a_0 alteration in the manner that fulfills this extended BVS rule, allowing for each cation to deviate from its nominal charge and Shannon's r_C state to some extent, as seen in Fig. 8.

4 Conclusion

This paper proposed a new extended lattice-parameter (a_0(ss)) model for stabilized zirconia (hafnia) with strong pyrochlore-type ordering and its associated broad a_0(ss) hump, by upgrading its previous version for parent fluorite-type solid solutions. With full use of several key Ln (Eu, Gd)-Mössbauer, EXAFS and MAS-NMR local-structure data, the two key structural facts, i.e., P-type extra a_0 distortional dilation at $y = 0.50$ (Fig. 1a) and non-Shannonian counteractive cation-radii (r_C) alterations in the initially-stabilized lower y range (Fig. 6), are identified and incorporated into the model. We could thus successfully devise the F-P-C ternary a_0(ss) model that can near quantitatively describe their strongly sigmoid a_0(ss) behaviour, revealing some intriguing new crystal as well as local-structure features and problems of these defective solid solutions. We have also proposed a new extended bond-valence sum rule as such non-Shannonian r_C alteration mechanism. The proposed extended a_0(ss) model is a primitive phenomenological one, needing much elaborations in the future: Its two major issues are (a) to build it on the more concrete basis of crystal and local structural reality of ordered pyrochlore (Fig. 2) and (b) to further integrate the F-C binary and F-P-C ternary models into a more unified one for the whole defect-fluorite oxides, either parent fluorite- or stabilized-type.

References

1. Nakamura, A.: Solid State Ionics **181**, 1543 (2010)
2. Nakamura, A.: Solid State Ionics **181**, 1631 (2010)
3. Otobe, H., Nakamura, A.: SOFC-VI, The Electrochem. Soc. Proc. 99–19, pp. 463–473 (1999)
4. Nakamura, A., Masaki, N., Otobe, H., Hinatsu, Y., Wang, J., Takeda, M.: Pure Appl. Chem. **79**, 1691 (2007)
5. Wang, J., Takeda, M., Shishido, T.: J. Nucl. Mater. **340**, 52 (2005)
6. Wang, J., Otobe, H., Nakamura, A., Takeda, M.: J. Solid State Chem. **176**, 105 (2003)
7. Wang, J., Takeda, M., Nakamura, A.: J. Nucl. Mater. **340**, 33 (2005)
8. Nakamura, A., Otobe, H., Wang, J., Takeda, M.: J. Phys. Chem. Solids **66**, 35 (2005)
9. Harada, D., Hinatsu, Y., Masaki, N., Nakamura, A.: J. Am. Ceram. Soc. **85**, 647–652 (2002)
10. Masaki, N.M., Otobe, H., Nakamura, A., Guillermo, N.R.D., Izumiyama, Y., Harada, D., Hinatsu, Y.: Hyperfine Interact. **C305**, 305–308 (2003)
11. Nakamura, A., Imai, K., Igawa, N., Okamoto, Y., Yamamoto, E., Matsukawa, S., Takahashi, M.: Hyperfine Inter. **207**, 67–71 (2012)
12. Kawata, K., Maekawa, H., Nemoto, T., Yamamura, T.: Solid State Ionics **177**, 1687–1690 (2006)
13. Maekawa, H., Kawata, K., Yamamura, T., Kawamura, J., Xiong, Y.P., Sakai, N., Yokokawa, H.: Solid State Ionics **180**, 313–319 (2009)
14. Kawada, K.: MS thesis, Graduate School of Engineering Tohoku University (2006)
15. Moriga, T., Emura, S., Yoshiasa, A., Kikkawa, S., Kanamaru, F., Koto, K.: Solid State Ionics **40–41**, 357–361 (1990)
16. Brown, I.D.: The Chemical Bond in Inorganic Chemistry. International Union of Crystallography Monographs of Crystallography, Oxford Univ. Press, Oxford (2002)